Journal of Materials Chemistry A

ROYAL SOCIETY OF CHEMISTRY

PAPER

View Article Online
View Journal | View Issue

Cite this: J. Mater. Chem. A, 2025, 13, 14172

Trimetallic spinel $NiCo_{2-x}Mo_xO_4$ oxygen evolution catalyst enabling bias-free solar water splitting with inverted perovskite solar cells†

Mahmoud G. Ahmed, ‡[a] Yi Fei Phang,‡[b] Ying Fan Tay,[c] Anupam Sadhu, [a] Pritish Mishra, [b] Akhmad Herman Yuwono[de] and Lydia H. Wong *[ab]

Efficient spinel oxide catalysts are pivotal for driving the oxygen evolution reaction (OER) for hydrogen production *via* solar-driven water splitting. Designing trimetallic spinel oxides with high-valence metal ions which leach out to promote surface reconstruction is an effective strategy to maximize active sites for the OER. Herein, we report a trimetallic spinel oxide, $NiCo_{2-x}Mo_xO_4$ as an efficient OER catalyst, generating 10 mA cm^{-2} at a low overpotential of 250 mV, and demonstrating stability for over 25 h. Experimental and spectroscopic results indicate that the partial leaching of Mo ions from tetrahedral sites in the electrolyte facilitates Ni^{2+} oxidation to Ni^{3+}, leading to the formation of an active nickel (oxy) hydroxide with numerous catalytic sites. Furthermore, integrating this spinel oxide in a 2-electrode water electrolyzer coupled with an inverted p-i-n perovskite solar cell enables bias-free solar water splitting with a solar-to-hydrogen efficiency of 8.8%. This work underscores the efficacy of using high-valence metal ions as effective dopants in activating spinel oxide pre-catalysts for the OER, thereby broadening their application in solar-driven water splitting technologies.

Received 21st November 2024
Accepted 27th March 2025

DOI: 10.1039/d4ta08267b

rsc.li/materials-a

Introduction

Sunlight as an endlessly renewable energy source, offers a beacon of hope for humanity in our collective endeavor to surmount the dual challenges of energy scarcity and environmental pollution. Efficient utilization of solar energy is pivotal in this pursuit, and photovoltaic (PV) cells stand out as a key technology for converting solar energy into electricity.[1] Recently, hybrid organic–inorganic metal halide perovskites have emerged as extremely promising candidates for the next wave of PV devices.[2,3] These materials exhibit unique features, including a high optical absorption coefficient, prolonged carrier lifetime, and ambipolar charge transport, resulting in a remarkable solar-to-electricity conversion efficiency surpassing 26%.[3,4] However, due to the intermittent and unpredictable nature of solar radiation, the need to store solar energy in chemical fuels becomes imperative, with hydrogen (H_2) emerging as the leading choice.[5] Integrated energy conversion–storage systems are proposed as highly effective routes to convert solar energy into chemical fuel.[6–8] In particular, the integrated PV cell with a water electrolysis system can efficiently produce green and recyclable hydrogen in a sustainable manner.[9]

Water electrolysis comprises two distinct half-reactions, the oxygen evolution reaction (OER) occurring at the anode and the hydrogen evolution reaction (HER) at the cathode.[10] The OER, with its inherent slow kinetics resulting from a four-electron transfer mechanism, is essential in various electrochemical energy conversion and storage devices, including water electrolysis and photoelectrochemical cells.[11,12] Consequently, extensive research endeavors have been focused on developing OER catalysts that exhibit high activity, durability, and cost-effectiveness.[11,13]

Exploring 3d transition metal oxides, particularly Ni and/or Co-based oxides, has garnered significant interest due to their good catalytic activity and stability.[14–16] The bimetallic spinel $NiCo_2O_4$, in particular, has demonstrated remarkable activity in the OER owing to its favorable electrical conductivity, high stability and possession of rich redox-active sites. Notably, spinel oxides containing Ni and/or Co have been reported to undergo a surface reconstruction process under electro-oxidation conditions leading to the formation of an active Ni and/or Co(oxy)hydroxide phase, respectively.[14] This surface

[a]Energy Research Institute @ NTU (ERI@N) Nanyang Technological University, Singapore 637553, Singapore. E-mail: lydiawong@ntu.edu.sg
[b]School of Materials Science and Engineering, Nanyang Technological University, Singapore 639798, Singapore
[c]Institute of Sustainability for Chemicals, Energy and Environment (ISCE^2), Agency for Science, Technology and Research (A*STAR), 1 Pesek Road Jurong Island, Singapore, 627833, Singapore
[d]Advanced Materials Research Center (AMRC), Faculty of Engineering, Universitas Indonesia, Indonesia
[e]Department of Metallurgical and Materials Engineering, Universitas Indonesia, Depok 16424, Indonesia

† Electronic supplementary information (ESI) available. See DOI: https://doi.org/10.1039/d4ta08267b

‡ These authors contributed equally to this work.

reconstruction is identified as a crucial step for maximizing the exposure of active sites, thereby enhancing OER catalysis. For instance, Wang *et al.* demonstrated that the Ni^{3+} enrichment on the surface of spinel $NiCo_2O_4$ is more active than Co, leading to the formation of active NiOOH for the OER.[14] Nevertheless, the performance of $NiCo_2O_4$ is still inferior due to the poor intrinsic activity and limited exposed active sites for the OER process. To address this limitation, several strategies have been proposed to activate the surface reconstruction and increase the density of exposed active sites for high OER activity. The formation of multimetallic spinel oxides is an effective strategy to increase the exposure of active sites.[17,18] For instance, the trimetallic $NiCo_{2-x}Fe_xO_4$ exhibits high catalytic performance (274 mV at 10 mA cm^{-2}) compared to $NiCo_2O_4$ (330 mV), attributed to the porous hollow structure, trimetallic composition and the surface reconstruction phenomenon of Ni^{2+} to $Ni^{3+}OOH$.[16] Liu *et al.* have reported that the OER activity of Cr-$NiCo_2O_4$ is higher than that of $NiCo_2O_4$, attributed to enhanced conductivity, enabling greater accessibility to active sites.[19]

Recent studies indicate that incorporating high-valence metals like Mo and W can trigger the surface reconstruction of a pre-catalyst into the active phase due to their leaching capabilities in alkaline medium, maximizing the number of active sites. For example, Fan *et al.* demonstrated that the sacrificial W facilitates the surface transformation of CoFe sulfide to CoFe (oxy)hydroxide, generating abundant active species.[20] Similarly, Dürr *et al.* observed that leaching of Mo ions from the $NiMoO_4 \cdot H_2O$ pre-catalyst promotes the formation of the active NiOOH phase.[21] Such observations highlight the benefits of using high-valence metal ions in other catalyst materials to promote the transformation of other pre-catalyst materials into active phases, enhancing the OER catalytic activity.

In the case of the spinel $NiCo_2O_4$ oxide as the pre-catalyst, the OER activity is often limited by the low exposure of Ni sites, particularly those in the tetrahedral sites. The incorporation of high-valence Mo^{6+} in tetrahedral sites introduces a unique advantage. Mo^{6+} can be selectively leached under alkaline conditions, creating cation vacancies, and significantly increasing the exposure of Ni sites for the OER. Consequently, forming a trimetallic spinel oxide $NiCo_{2-x}Mo_xO_4$ by incorporating high-valence Mo (*i.e.*, Mo^{6+}) is a promising strategy to generate numerous highly active sites and enhance the catalytic performance.

Herein, we report the synthesis of a trimetallic $NiCo_{2-x}Mo_xO_4$ spinel oxide by a facile hydrothermal method followed by one annealing step. Notably, the partial leaching of Mo increases the exposure of Ni active sites for the OER and triggers the self-surface reconstruction, forming the active nickel (oxy) hydroxide. The reconstructed spinel $NiCo_{2-x}Mo_xO_4$ ($x = 0.1$) oxide demonstrates high catalytic activity on Ni foam with a low overpotential of 250 mV at 10 mA cm^{-2} and a small Tafel slope of 41.5 mV dec^{-1}. By integrating the highly active OER catalyst ($NiCo_{2-x}Mo_xO_4$, $x = 0.1$) into the water electrolysis system, the overall voltage to drive water splitting was only 1.53 V at 10 mA cm^{-2}. The integration of the water electrolysis system with a p-i-n architecture perovskite solar cell enables an unbiased solar water splitting, achieving a solar-to-hydrogen efficiency of 8.8%.

Results and discussion

Bi/trimetallic spinel oxides ($NiCo_{2-x}Mo_xO_4$) were deposited directly on conductive fluorine-doped tin oxide (FTO) *via* a straightforward hydrothermal approach followed by annealing at 400 °C (more details are provided in the ESI†). The variation of Mo ratio in the trimetallic spinel oxide $NiCo_{2-x}Mo_xO_4$ shows a significant effect on the OER catalytic performance as shown in Fig. S1.† $NiCo_{2-x}Mo_xO_4$ with $x = 0.1$ demonstrates the highest catalytic performance, characterized by a low overpotential value. X-ray diffraction (XRD) patterns of bimetallic $NiCo_2O_4$ and trimetallic $NiCo_{1.9}Mo_{0.1}O_4$ are shown in Fig. 1a. The diffraction peaks of both $NiCo_2O_4$ and $NiCo_{1.9}Mo_{0.1}O_4$ matched well with that of the standard cubic spinel $NiCo_2O_4$ with a space group of $Fc\bar{3}m$ (JCPDS no. 20-0781). The XRD pattern of trimetallic $NiCo_{1.9}Mo_{0.1}O_4$ did not show any peak shift, which might be attributed to the low amount of Mo. Fig. 1b shows the polarization curves with *iR* correction for bimetallic $NiCo_2O_4$ and trimetallic $NiCo_{1.9}Mo_{0.1}O_4$ catalysts. Fig. S2† shows the polarization curves of oxides without *iR* correction. $NiCo_2O_4$ achieves a current density of 10 mA cm^{-2} with an overpotential of 460 mV, whereas $NiCo_{1.9}Mo_{0.1}O_4$ achieves the same current density with only 328 mV (Fig. 1c). The Tafel slope values for these spinel oxides are derived from the polarization curves shown in Fig. 1d. The Tafel slope of trimetallic $NiCo_{1.9}Mo_{0.1}O_4$ (59.6 mV dec^{-1}) is much lower than that of bimetallic $NiCo_2O_4$ (176.7 mV dec^{-1}), indicating improved surface reaction kinetics. Generally, a Tafel slope of 120 mV dec^{-1} or higher suggests that the rate-limiting step (RLS) in the OER process is the adsorption of OH^-, as observed with $NiCo_2O_4$. In contrast, the lower Tafel slope of $NiCo_{1.9}Mo_{0.1}O_4$, closer to 40 mV dec^{-1}, indicates that the RLS is the formation of MOOH.[10] This shift in the RLS is likely responsible for the enhanced OER performance of the trimetallic oxide, which benefits from accelerated reaction kinetics and better OH^- adsorption.

The morphology of spinel $NiCo_2O_4$ and $NiCo_{1.9}Mo_{0.1}O_4$ is investigated by scanning electron microscopy (SEM) and high-resolution transmission electron microscopy (HR-TEM). SEM images show that $NiCo_2O_4$ comprises a hybrid of 2-dimensional (2D) nanosheets and 1D nanowires (Fig. 2a and S3a†). HR-TEM further provides a closer examination of the nanowires (Fig. 2b). The HR-TEM image of $NiCo_2O_4$ displays distinct lattice fringes with an interplanar spacing (d) of 0.29 nm, corresponding to the (220) lattice plane of spinel $NiCo_2O_4$ (Fig. 2c and d). Additionally, the selected area electron diffraction (SAED) pattern (Fig. S3b†) confirms the polycrystalline nature of spinel $NiCo_2O_4$. In contrast, trimetallic $NiCo_{1.9}Mo_{0.1}O_4$ exhibits 3D flower-like microstructures (Fig. S4†) composed of interconnected 1D nanowires as shown in Fig. 2e and f. The variation in the morphology of $NiCo_2O_4$ and $NiCo_{1.9}Mo_{0.1}O_4$ can be explained by the decomposition of ammonium molybdate (Mo precursor) to release ammonia which changes the solution pH and thus the degree of supersaturation and the morphology.[22] HR-TEM confirms the high crystallinity of $NiCo_{1.9}Mo_{0.1}O_4$ as

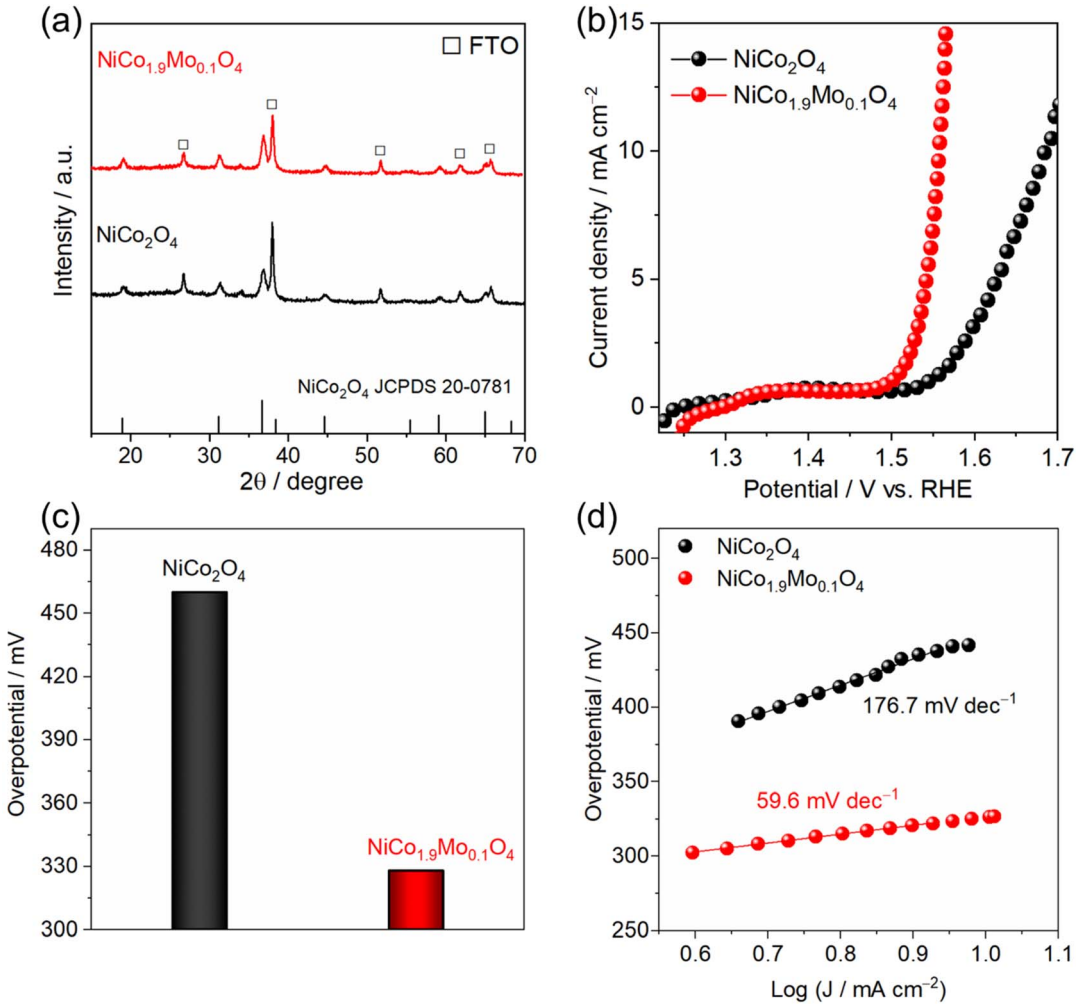

Fig. 1 (a) XRD pattern of $NiCo_2O_4$ and $NiCo_{1.9}Mo_{0.1}O_4$ deposited on FTO substrates. (b) Polarization curves of $NiCo_2O_4$ and $NiCo_{1.9}Mo_{0.1}O_4$ after *iR* correction. (c) Overpotential values of $NiCo_2O_4$ and $NiCo_{1.9}Mo_{0.1}O_4$ at 10 mA cm^{-2}. (d) Tafel plots of $NiCo_2O_4$ and $NiCo_{1.9}Mo_{0.1}O_4$ derived from LSV scans.

shown in Fig. 2g and h. Furthermore, energy dispersive X-ray spectroscopy (EDS) verifies the existence of Mo, Co, Ni and O, while the elemental mapping images additionally illustrate their uniform distribution in $NiCo_{1.9}Mo_{0.1}O_4$ (Fig. 2i and S5†). Similarly, EDS mapping of $NiCo_2O_4$ reveals a homogeneous elemental distribution (Fig. S6†). The atomic ratio of Ni and Co in $NiCo_2O_4$ is determined to be about 1 : 2 (Table S1†). Similarly, in $NiCo_{1.9}Mo_{0.1}O_4$, the atomic ratio of Ni to the sum of Mo and Co is approximately 1 : 2, aligning with the intended target composition (Table S1†).

Compared to 2D-$NiCo_2O_4$, the 3D morphology of $NiCo_{1.9}Mo_{0.1}O_4$ maximizes the exposed active sites at the surface and increases the contact area with the electrolyte, thereby enhancing the OER catalytic performance.[23] The active surface area is further evaluated by the measurements of double-layer capacitance (C_{dl}) (Fig. S7 and S8†). C_{dl}, which correlates with the active surface area, serves as an indicator for estimating the electrochemical active surface area (ECSA). 3D-$NiCo_{1.9}Mo_{0.1}O_4$ exhibits a significantly higher surface area, approximately twice that of 2D-$NiCo_2O_4$. To ensure a fair assessment of the catalyst, the impact of morphology is excluded by normalizing the OER performance with respect to ECSA. The ECSA-normalized specific activity in Fig. S8b† demonstrates that at $\eta = 300$ mV, $NiCo_{1.9}Mo_{0.1}O_4$ exhibits a high specific activity (0.01 mA cm_{ECSA}^{-2}), which is 3 times higher than that of $NiCo_2O_4$ (0.003 mA cm_{ECSA}^{-2}). This highlights the effective role of Mo in boosting the catalytic performance of spinel $NiCo_2O_4$.

To gain insight into the effect of Mo on the electronic structure of the spinel oxide, we conducted X-ray photoelectron spectroscopy (XPS) measurements on both $NiCo_2O_4$ and $NiCo_{1.9}Mo_{0.1}O_4$. Fig. 3a shows the XPS spectra of Co 2p core level, consisting of two characteristic peaks Co $2p_{3/2}$ at ≈779.5 eV and Co $2p_{1/2}$ at ≈795.0 eV along with their corresponding shakeup satellites. Due to the proximity of $2p_{1/2}$ and $2p_{3/2}$ peak locations for Co^{2+} and Co^{3+}, the satellite features and their intensity were analyzed using a series of standard components (*i.e.*, 787 eV for $Co(OH)_2$-like Co^{2+} and 789.5 eV for Co_3O_4 with dominant Co^{3+}) as shown in Fig. 3a.[24] Therefore, the Co^{2+} to Co^{3+} ratio is determined based on their respective compositions. Fig. 3a shows that the Co^{3+} is the predominant

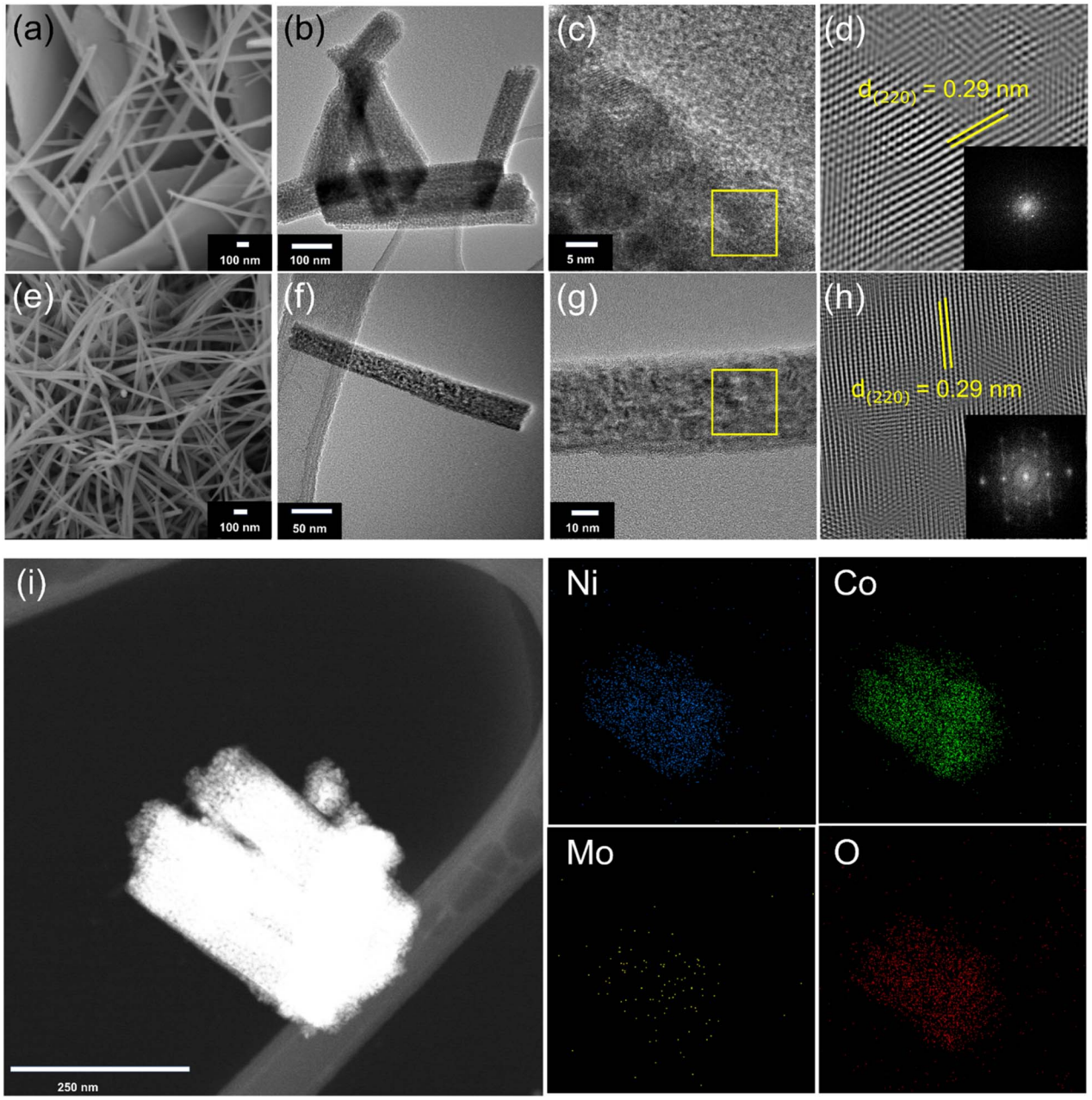

Fig. 2 (a and b) SEM and HR-TEM images of $NiCo_2O_4$. (c and d) HR-TEM of $NiCo_2O_4$ showing the crystal lattice fringes. (e and f) SEM and HR-TEM images of $NiCo_{1.9}Mo_{0.1}O_4$. (g and h) HR-TEM of $NiCo_{1.9}Mo_{0.1}O_4$ showing the crystal lattice fringes. (i) EDS atomic elemental mapping of trimetallic $NiCo_{1.9}Mo_{0.1}O_4$.

oxidation state in both $NiCo_2O_4$ and $NiCo_{1.9}Mo_{0.1}O_4$ (Fig. 3b and S9†). However, in $NiCo_{1.9}Mo_{0.1}O_4$, the $Co(OH)_2$-like Co^{2+} at 787 eV is slightly decreased indicating more Co^{3+}. The fitting results are summarized in Fig. 3b. Fig. 3c shows that the XPS spectrum of Mo 3d is dominated by the high valence state, *i.e.*, Mo^{6+} and Mo^{5+}. The partial reduction of Mo^{6+} to Mo^{5+} might be explained by the electron exchange occurring between Co^{2+} and Mo^{5+} as follows: $Mo^{6+} + Co^{2+} \leftrightarrow Mo^{5+} + Co^{3+}$.[25] The cation redistribution of Co^{2+} and Mo^{6+} can explain the slight decrease of Co^{2+} ratios which is induced by the occupancy of Mo^{6+} in tetrahedral sites in $NiCo_{1.9}Mo_{0.1}O_4$.[26,27]

The XPS spectra of Ni 2p in $NiCo_2O_4$ and $NiCo_{1.9}Mo_{0.1}O_4$ are also shown in Fig. 3d. The spectral line of Ni 2p of $NiCo_{1.9}Mo_{0.1}O_4$ closely resembles that of $NiCo_2O_4$, suggesting an insignificant change in Ni^{2+}/Ni^{3+} ratio in both spinel oxides. The fitting results are further summarized in Fig. 3e and S10.† Additionally, the O 1s XPS spectra for these spinel oxides are shown in Fig. S11.† Comparatively, the O 1s XPS spectrum of $NiCo_{1.9}Mo_{0.1}O_4$ shows negligible change compared to that of $NiCo_2O_4$. The O 1s XPS spectra of both oxides can be deconvoluted into 4 peaks as shown in Fig. 3f. These peaks correspond to: lattice oxygen species (M–O) at 529.2 eV, oxygen defects

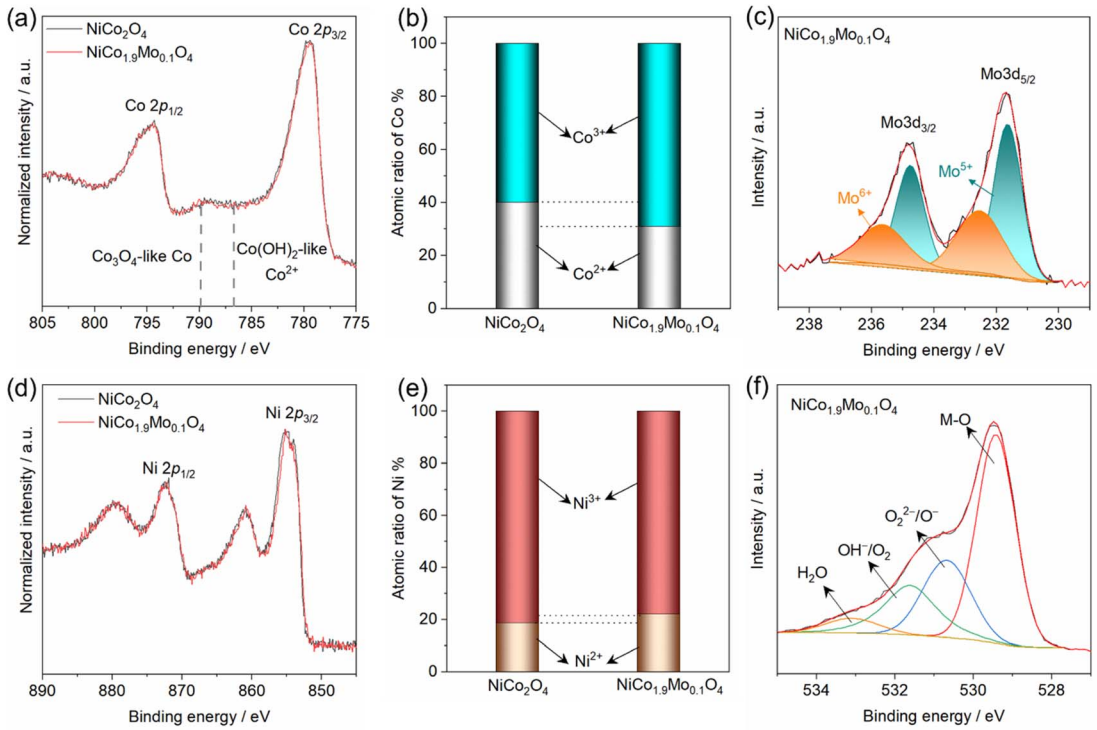

Fig. 3 XPS spectra of (a) Co 2p in $NiCo_2O_4$ and $NiCo_{1.9}Mo_{0.1}O_4$, (b) atomic ratios of Co^{2+} and Co^{3+} in oxides, (c) XPS spectra of Mo 3d in $NiCo_{1.9}Mo_{0.1}O_4$, (d) XPS spectra of Ni 2p in $NiCo_2O_4$ and $NiCo_{1.9}Mo_{0.1}O_4$, (e) atomic ratios of Ni^{2+}/Ni^{3+} in oxides and (f) O 1s XPS in $NiCo_{1.9}Mo_{0.1}O_4$.

(O_2^{2-}/O^-), hydroxyl group (OH^-/O_2) at 531.4 eV and molecular water (H_2O) at 532.5 eV.[28]

Spinel oxides are widely recognized as pre-catalysts for the OER, undergoing surface reconstruction under anodic potential to form the true active species.[17] This reconstruction involves the pre-oxidation of cations with low oxidation states to higher oxidation states, which is a key step in forming the active (oxy)hydroxide phase. Cyclic voltammetry (CV) is commonly used to both induce and monitor this electrochemical activation, providing insights into the surface changes and formation of active species. The CV profiles of $NiCo_2O_4$ and $NiCo_{1.9}Mo_{0.1}O_4$ are shown in Fig. 4a. The polarization curves of $NiCo_2O_4$ and $NiCo_{1.9}Mo_{0.1}O_4$ show a distinct redox couple peak at ≈1.45 V *vs.* RHE, corresponding to the oxidation of Ni species ($Ni^{2+} \rightarrow Ni^{3+}$).[29,30] However, in the case of $NiCo_{1.9}Mo_{0.1}O_4$, the CV curve exhibits a significantly higher and broader profile than that of $NiCo_2O_4$, suggesting the substantial generation of active Ni species. This indicates that Mo accelerates the self-activation/reconstruction process. Notably, the Ni^{2+}/Ni^{3+} redox peak gradually increases and stabilizes after the 47th cycle, signifying a stable steady state and indicating the successful completion of activation (Fig. S12†).[30] This incremental rise is attributed to the progressive generation of active NiOOH and a growing abundance of accessible catalytically active sites in $NiCo_{1.9}Mo_{0.1}O_4$. Consequently, CV cycling accelerates the reconstruction and self-activation processes, resulting in the exposure of a greater number and density of active sites.

XPS was employed to monitor the surface chemical states after the OER to further identify the real active sites in $NiCo_{1.9}Mo_{0.1}O_4$ for the OER. The peaks at 855 eV and 857.6 eV correspond to Ni^{2+} and Ni^{3+} states present in $NiCo_{1.9}Mo_{0.1}O_4$ (Fig. S13†). The calculated Ni^{3+}/Ni^{2+} ratios of $NiCo_{1.9}Mo_{0.1}O_4$ is increased by 2.6-fold after the OER (Fig. 4b). This significant variation in ratios reveals the surface changes of $NiCo_{1.9}Mo_{0.1}O_4$ during the OER process, forming active NiOOH species, contributing to enhanced catalytic activity. Conversely, a minor change is observed in the Co 2p states for $NiCo_{1.9}Mo_{0.1}O_4$ before and after the OER (Fig. S14†). The calculated Co^{2+}/Co^{3+} ratio was almost the same before and after the OER, as shown in Fig. S15.† This suggests that Co persists as a mixture of Co^{2+}/Co^{3+} during the OER. Surface atomic ratio calculations further reveal the partial leaching of Mo after the OER, whereas Ni and Co remain unchanged (Fig. 4c).

Furthermore, to determine whether the enhanced OER activity arises from the incorporation of Mo in spinel oxide or the presence of trace Fe impurities in the electrolyte, OER activity was evaluated in 0.1 M ultrapure KOH electrolyte and unpurified KOH containing Fe (<0.0005%). The LSV curves (Fig. S16†) show nearly identical OER activity in both electrolytes, indicating that Fe impurities have no significant effect on the measurements. This further confirms that the enhanced activity of trimetallic $NiCo_{1.9}Mo_{0.1}O_4$ stems from Mo incorporation.

Based on the aforementioned results, Ni^{2+} ions play a more active role than Co^{2+} and Co^{3+} in tetrahedral and octahedral

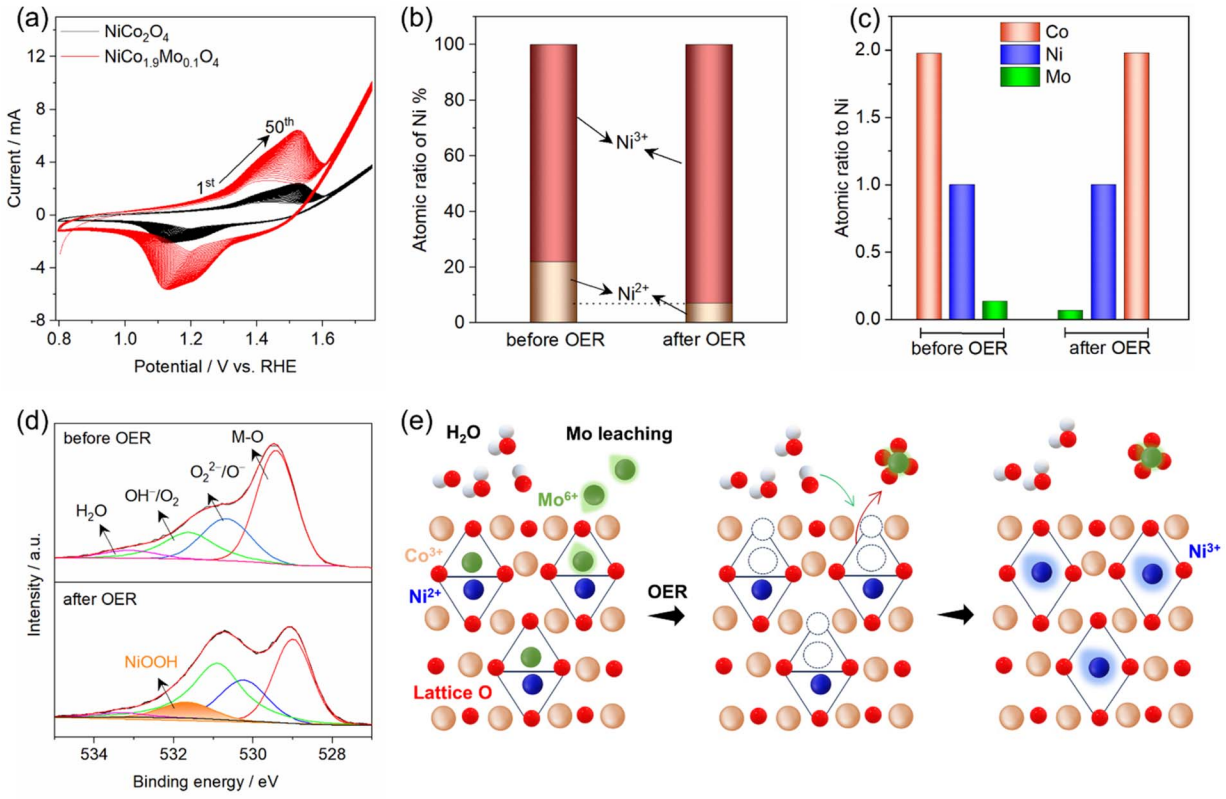

Fig. 4 (a) CV measurements of $NiCo_2O_4$ and $NiCo_{1.9}Mo_{0.1}O_4$ (50 cycles), (b) atomic ratios of Ni^{2+} and Ni^{3+} in $NiCo_{1.9}Mo_{0.1}O_4$ before and after the OER, (c) surface atomic concentration of Co, Ni and Mo, (d) O 1s XPS spectra in $NiCo_{1.9}Mo_{0.1}O_4$ before and after the OER, (e) schematic illustration of surface transformation in $NiCo_{1.9}Mo_{0.1}O_4$ showing Mo^{6+} leaching, cation vacancies, and NiOOH formation.

sites, respectively, within spinel oxides.[14] This result is supported by the gradual increase of Ni^{2+}/Ni^{3+} redox pairs from CV curves (Fig. 4a). However, in $NiCo_2O_4$, the number of active Ni sites was limited as indicated by the weak anodic peak. In contrast, in $NiCo_{1.9}Mo_{0.1}O_4$, the high valence Mo^{6+} ions replace the tetrahedral Co^{2+} ions. Under anodic conditions in an alkaline medium (pH ≈ 14), these Mo^{6+} ions partially leach out, as predicted by the Pourbaix diagram.[31] Surface hydroxylation promotes the dissolution of Mo^{6+} as MoO_4^{2-} ($Mo^{6+}O_3 + OH^- \rightarrow MoO_4^{2-} + H_2O$), particularly at high anodic potentials. The partial leaching of Mo^{6+}, along with the loss of lattice oxygen, generates cation and anion vacancies in the tetrahedral sites (Fig. 4e), triggering surface rearrangement, and increasing Ni^{2+} exposure for the OER as evidenced by the CV curves (Fig. 4a). The highly exposed Ni^{2+} ions react with OH^- ions from the electrolyte, forming a hydroxide layer that is subsequently electro-oxidized to form the active layer of amorphous NiOOH. The formation of NiOOH is confirmed by post-OER XPS, where a new peak appears in the O 1s spectrum (Fig. 4d). Furthermore, HR-TEM imaging (Fig. S17†) provides direct structural evidence of this transformation, revealing a distinct difference between the crystalline spinel oxide and the amorphous NiOOH domains. Fast Fourier-transform (FFT) patterns obtained from the yellow and white squares further confirm the structural changes, with the yellow square (dark regions) reflecting the high crystallinity of the spinel oxide, while the white square (light regions) exhibits the highly disordered nature of amorphous NiOOH. EDS mapping further reveals the distribution of Ni and Co, with Mo retained at ≈60% of its initial concentration after partial leaching (Fig. S18†). The schematic of the proposed mechanism is shown in Fig. 4e.

Nevertheless, the catalytic role of Co ions cannot be dismissed entirely, as the behavior of Ni cation might be affected by the presence of coordinated Co cations and oxygen anions in the surrounding environment. Additionally, Co oxide serves as a structural support, providing a conductive matrix for charge carriers.[14]

Motivated by the promising performance of $NiCo_{1.9}Mo_{0.1}O_4$/FTO as an effective electrocatalyst, we extended our investigation to include the deposition of $NiCo_{1.9}Mo_{0.1}O_4$ on 3D-interconnected porous and conducting nickel foam (NF). The SEM images of $NiCo_2O_4$ and $NiCo_{1.9}Mo_{0.1}O_4$ on NF show nanorods and nanowires, respectively (Fig. S19†). It is noteworthy that the morphology of $NiCo_{1.9}Mo_{0.1}O_4$ remains the same as on FTO (Fig. 2d and S19c†). The OER activity of $NiCo_2O_4$ and $NiCo_{1.9}Mo_{0.1}O_4$ on NF in 1 M KOH is shown in Fig. 5a. $NiCo_{1.9}Mo_{0.1}O_4$/NF achieves a current density of 10 and 500 mA cm^{-2} at a remarkable low overpotential values of 250 and 320 mV, respectively. In contrast, $NiCo_2O_4$/NF demonstrated poor catalytic activity for the OER with an overpotential

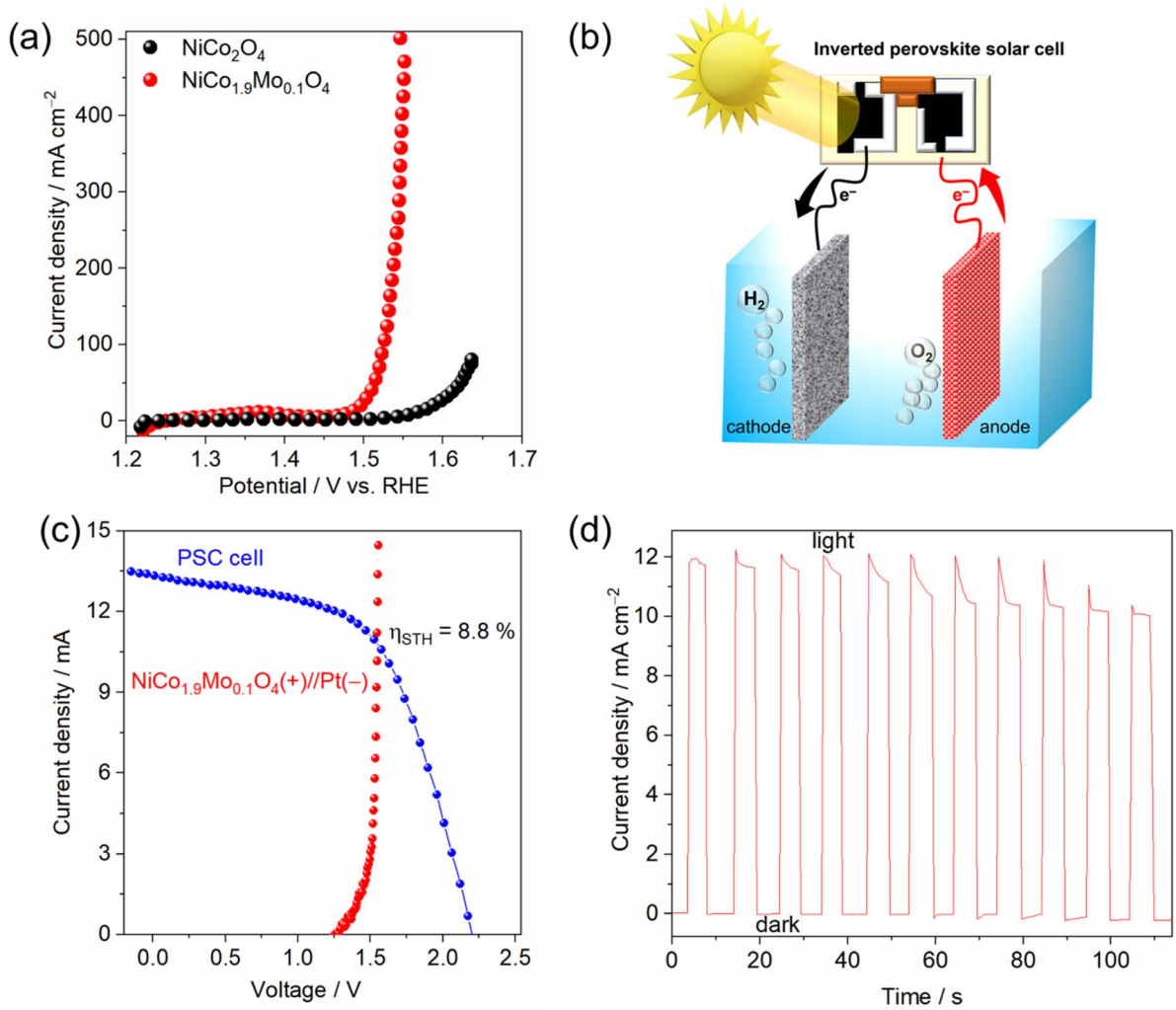

Fig. 5 (a) Polarization curves of $NiCo_2O_4$/NF and $NiCo_{1.9}Mo_{0.1}O_4$/NF, (b) schematic illustration of the PSC-driven water electrolysis, (c) current–voltage curves of the perovskite solar cell under 1 sun illumination (AM 1.5 G, 100 mW cm^{-2}) and /NF in a two-electrode cell configuration, (d) current–time plot of the water electrolysis system without external bias potential ($V = 0$) under 1 sun illumination.

of 330 mV at 10 mA cm^{-2}. The Tafel slope for $NiCo_{1.9}Mo_{0.1}O_4$/NF was 41.5 mV dec^{-1}, which is lower than that of $NiCo_2O_4$ (73 mV dec^{-1}) as shown in Fig. S20.† The specific activity of $NiCo_{1.9}Mo_{0.1}O_4$ on NF is still high compared to $NiCo_2O_4$ on the same substrate (Fig. S21†). The $NiCo_{1.9}Mo_{0.1}O_4$/NF maintains continuous operation for over 25 h under electrochemical OER conditions with a negligible change in current density (Fig. S22†). Notably, the morphology remains largely unchanged after the stability test (Fig. S23†), demonstrating the high structural stability of the oxide.

Inspired by the high catalytic activity observed in $NiCo_{1.9}Mo_{0.1}O_4$/NF for the OER, we utilized this activity of the OER catalyst in a photovoltaic (PV)–water electrolysis integrated system. The water electrolysis cell consisted of a 2-electrode system, featuring a platinum (Pt) cathode for the HER and KOH as the electrolyte (Fig. 5b). The Pt/NF//$NiCo_{1.9}Mo_{0.1}O_4$/NF cell requires only 1.53 V to generate 10 mA cm^{-2}, surpassing most reported catalysts or even comparable to noble-based catalysts (Table S2†). The solar water splitting system was fabricated by integrating this cell with an inverted perovskite solar cell (Fig. 5b), with its detailed structure shown in Fig. S24a.† The inverted perovskite solar cell demonstrated a short circuit current density (J_{SC}) of 18.12 mA cm^{-2} and an open-circuit voltage (V_{OC}) of 1.03 V (Fig. S24b†). It achieved a power conversion efficiency (PCE) of ≈13% with a fill factor (FF) of ≈70%. However, since 1.03 V voltage is not sufficient for driving the water splitting reaction, two solar cell devices were connected in series to generate the required voltage. Connecting the series-configured inverted perovskite solar cell and water electrolysis cell with a wire (Fig. 5b and S25†) enabled the PV–water electrolyzer system to drive the overall water splitting without an external bias, operating at a current density of ≈11 mA cm^{-2} under standard AM 1.5 G sunlight (Fig. 5c, d and ESI Video†). A solar to hydrogen efficiency (STH) of 8.8% is achieved. It should be noted that the STH can be improved to a higher value with the improvement of perovskite solar cell efficiency.

Conclusions

In summary, we have successfully synthesized a trimetallic spinel oxide $NiCo_{2-x}Mo_xO_4$ with nanowire morphology using a facile hydrothermal method followed by one-step annealing. Electrochemical measurements and electronic structure analyses reveal that the surface of spinel $NiCo_{2-x}Mo_xO_4$ ($x = 0.1$) undergoes reconstruction to form the active phase, nickel (oxy) hydroxide. This transformation is induced by partial leaching of Mo cations, increasing the exposure of more active sites to the OER. Consequently, the oxide exhibits high catalytic activity, with a low overpotential of 250 mV at 10 mA cm^{-2} and high stability for over 25 h in alkaline medium. Additionally, when integrated with an inverted perovskite solar cell, the trimetallic spinel oxide enables bias-free solar water splitting, reaching 8.8% solar-to-hydrogen efficiency. This study highlights the role of metal ions with leaching capabilities to enhance the OER activity of spinel oxides and expand their application for photovoltaic-driven water splitting.

Data availability

The data supporting this article have been included as part of the ESI.†

Author contributions

Mahmoud G. Ahmed: conceptualization, writing-original draft, synthesis, characterization of oxides, electrochemical measurements. Yi Fei Phang: synthesis, electrochemical measurements. Y. F. Tay: XPS analysis. Anupam Sadhu: fabrication of the perovskite solar cell device. Pritish Mishra: TEM characterization. Akhmad Herman Yuwono: writing-reviewing and editing; Lydia H. Wong: conceptualization, validation, supervision, administration, writing-reviewing and editing and funding.

Conflicts of interest

There are no conflicts to declare.

Acknowledgements

This work was partially supported by Singapore Ministry of Education (MOE) AcRF Tier 2 grant (MOE T2EP50120-00081) and Tier 1 grant (2020-T1-001-147 (RG64/20)). Additionally, we would like to acknowledge the Indonesian Endowment Fund for Education (LPDP) on behalf of the Indonesian Ministry of Education, Culture, Research, and Technology, managed under the INSPIRASI Program (Grant No. PRJ-61/LPDP/2022 and 612/E1/KS.06.02/2022).

References

1 G. K. Singh, *Energy*, 2013, **53**, 1–13.
2 A. Sadhu, M. Rai, T. Salim, X. Jin, J. M. R. Tan, S. W. Leow, M. G. Ahmed, S. Magdassi, S. G. Mhaisalkar and L. H. Wong, *Adv. Funct. Mater.*, 2021, **31**, 2103807.
3 A. S. R. Bati, Y. L. Zhong, P. L. Burn, M. K. Nazeeruddin, P. E. Shaw and M. Batmunkh, *Commun. Mater.*, 2023, **4**, 2.
4 NREL, **https://www.nrel.gov/pv/interactive-cell-efficiency.html**, (accessed July, 2024).
5 T. J. Jacobsson, V. Fjällström, M. Edoff and T. Edvinsson, *Energy Environ. Sci.*, 2014, **7**, 2056–2070.
6 H. L. Tuller, *Mater. Renew. Sustain. Energy*, 2017, **6**, 3.
7 Z. Li, S. Fang, H. Sun, R.-J. Chung, X. Fang and J.-H. He, *Adv. Energy Mater.*, 2023, **13**, 2203019.
8 J. Chen, C. Dong, H. Idriss, O. F. Mohammed and O. M. Bakr, *Adv. Energy Mater.*, 2020, **10**, 1902433.
9 B. Weng, F. Xu, C. Wang, W. Meng, C. R. Grice and Y. Yan, *Energy Environ. Sci.*, 2017, **10**, 121–128.
10 N.-T. Suen, S.-F. Hung, Q. Quan, N. Zhang, Y.-J. Xu and H. M. Chen, *Chem. Soc. Rev.*, 2017, **46**, 337–365.
11 M. G. Ahmed, Y. F. Tay, X. Chi, M. Zhang, J. M. R. Tan, S. Y. Chiam, A. Rusydi and L. H. Wong, *Small*, 2023, **19**, 2204520.
12 M. G. Ahmed, M. Zhang, Y. F. Tay, S. Y. Chiam and L. H. Wong, *ChemSusChem*, 2020, **13**, 5489–5496.
13 M. G. Ahmed, Y. F. Tay, X. Chi, A. S. Razeen, Y. Fang, M. Zhang, A. Sng, S. Y. Chiam, A. Rusydi and L. H. Wong, *Angew. Chem., Int. Ed.*, 2025, **64**, e202416757.
14 H.-Y. Wang, Y.-Y. Hsu, R. Chen, T.-S. Chan, H. M. Chen and B. Liu, *Adv. Energy Mater.*, 2015, **5**, 1500091.
15 X. Gao, H. Zhang, Q. Li, X. Yu, Z. Hong, X. Zhang, C. Liang and Z. Lin, *Angew. Chem., Int. Ed.*, 2016, **55**, 6290–6294.
16 Y. Huang, S. L. Zhang, X. F. Lu, Z.-P. Wu, D. Luan and X. W. Lou, *Angew. Chem., Int. Ed.*, 2021, **60**, 11841–11846.
17 L. Gao, X. Cui, C. D. Sewell, J. Li and Z. Lin, *Chem. Soc. Rev.*, 2021, **50**, 8428–8469.
18 M. G. Ahmed, Y. F. Tay, M. Zhang, S. Y. Chiam and L. H. Wong, *ACS Mater. Lett.*, 2024, 4756–4764, DOI: **10.1021/acsmaterialslett.4c00857**.
19 T. Liu and P. Diao, *Nano Res.*, 2020, **13**, 3299–3309.
20 K. Fan, H. Zou, Y. Ding, N. V. R. A. Dharanipragada, L. Fan, A. K. Inge, L. Duan, B. Zhang and L. Sun, *Small*, 2022, **18**, 2107249.
21 R. N. Dürr, P. Maltoni, H. Tian, B. Jousselme, L. Hammarström and T. Edvinsson, *ACS Nano*, 2021, **15**, 13504–13515.
22 D. T. Phat, P. M. Thao, N. Van Nghia, L. T. Son, T. V. Thu, N. T. Lan, N. Q. Quyen, N. Van Ky and T. Van Nguyen, *J. Energy Storage*, 2021, **33**, 102030.
23 P. Sun, Y. Zhou, H. Li, H. Zhang, L. Feng, Q. Cao, S. Liu, T. Wågberg and G. Hu, *Appl. Catal., B*, 2022, **310**, 121354.
24 M. C. Biesinger, B. P. Payne, A. P. Grosvenor, L. W. M. Lau, A. R. Gerson and R. S. C. Smart, *Appl. Surf. Sci.*, 2011, **257**, 2717–2730.
25 T. Mazari, C. R. Marchal, S. Hocine, N. Salhi and C. Rabia, *J. Nat. Gas Chem.*, 2010, **19**, 54–60.
26 J. M. Byrne, V. S. Coker, E. Cespedes, P. L. Wincott, D. J. Vaughan, R. A. D. Pattrick, G. van der Laan, E. Arenholz, F. Tuna, M. Bencsik, J. R. Lloyd and N. D. Telling, *Adv. Funct. Mater.*, 2014, **24**, 2518–2529.

27 G. D. Dwivedi, K. F. Tseng, C. L. Chan, P. Shahi, J. Lourembam, B. Chatterjee, A. K. Ghosh, H. D. Yang and S. Chatterjee, *Phys. Rev. B*, 2010, **82**, 134428.
28 C. Yuan, J. Li, L. Hou, X. Zhang, L. Shen and X. W. Lou, *Adv. Funct. Mater.*, 2012, **22**, 4592–4597.
29 L. Trotochaud, J. K. Ranney, K. N. Williams and S. W. Boettcher, *J. Am. Chem. Soc.*, 2012, **134**, 17253–17261.
30 S. Hou, W. Li, S. Watzele, R. M. Kluge, S. Xue, S. Yin, X. Jiang, M. Döblinger, A. Welle, B. Garlyyev, M. Koch, P. Müller-Buschbaum, C. Wöll, A. S. Bandarenka and R. A. Fischer, *Adv. Mater.*, 2021, **33**, 2103218.
31 M. Nishimoto, I. Muto, Y. Sugawara and N. Hara, *J. Electrochem. Soc.*, 2019, **166**, C3081.